

See discussions, stats, and author profiles for this publication at: <https://www.researchgate.net/publication/231274425>

Optimization of Channel Width Distribution of a Gas Flow Field by Integrating Computational Fluid Dynamics Code with a Simplified Conjugate-Gradient Method

ARTICLE *in* ENERGY & FUELS · NOVEMBER 2009

Impact Factor: 2.79 · DOI: 10.1021/ef9007455

CITATIONS

5

READS

18

3 AUTHORS, INCLUDING:



Chin-Hsiang Cheng

National Cheng Kung University

137 PUBLICATIONS **1,845** CITATIONS

SEE PROFILE



Yu-Xian Huang

18 PUBLICATIONS **244** CITATIONS

SEE PROFILE

Optimization of Channel Width Distribution of a Gas Flow Field by Integrating Computational Fluid Dynamics Code with a Simplified Conjugate-Gradient Method

Jiin-Yuh Jang,[†] Chin-Hsiang Cheng,^{*,‡} and Yu-Xian Huang[†]

[†]Department of Mechanical Engineering, [‡]Department of Aeronautics and Astronautics, and National Cheng-Kung University, Tainan, Taiwan 70101, Republic of China

Received July 19, 2009. Revised Manuscript Received October 25, 2009

This study is aimed at development of an approach applied for optimal design of straight channel width distribution that leads to an even flow field used in a micro-reformer by computational optimization. The approach is developed by integrating a direct problem solver with an optimizer. A commercial computational fluid dynamics code (CFD-ACE+) is used as the direct problem solver, which is used to predict the three-dimensional mass and momentum transport phenomenon in the flow field. On the other hand, the simplified conjugate-gradient method (SCGM) is employed as the optimizer, which works with the direct problem solver on optimization of the channel width distribution. The design of straight channel width distribution that leads to an even channel flow rate distribution is attempted. In this study, the optimization of a flow field is carried out, which has three different models regarding the inlet and outlet configuration, including (1) central inlet/central outlet, (2) right inlet/right outlet, and (3) right inlet/left outlet. Results show that, for the three models considered, the standard deviation of the flow rates in the channels for models 1, 2, and 3 are reduced from 0.22, 0.55, and 0.18 to 0.005, 0.013, and 0.0068, respectively.

1. Introduction

Fuel cells need hydrogen or hydrogen-rich feed gas as fuel. Several proven technologies, such as steam reforming, auto-thermal reforming, partial oxidation, and water–gas shift, can be used to extract hydrogen from fuels, such as gasoline, diesel, liquid petroleum gas, methane, ethanol, and methanol. Among them, methanol is an attractive fuel for hydrogen production because of its low reforming temperatures, low steam/carbon ratio, good miscibility with water, and low content of sulfur compounds. The steam-reforming process for methanol is represented by the following equations:¹

Steam reforming of methanol:



Methanol decomposition:



Water–gas shift reaction:



A typical catalytic steam-reforming system integrates the endothermic methanol steam reforming with the exothermic combustion of methanol or hydrogen-containing gas from the fuel cell. The feed for the reformer/combustor system consists of vaporized methanol and water. Part of the methanol vapor and/or hydrogen from the fuel cell anode off gas is mixed with air and catalytically combusted in the combustion section of the system to generate the heat for the steam reforming of

methanol in the reforming section. The hot flue gas from the combustor can be used to heat up water and methanol.

A micro-reformer system, consisting of a smaller scale vaporizer, a combustor, and a steam reformer, can be used as a sustained source of hydrogen for proton-exchange membrane fuel cells (PEMFCs) through the catalytic steam reformation of methanol. A microreformer in combination with a micro fuel cell is proposed as an alternative to conventional portable sources of electricity, such as batteries, because of its ability to provide an uninterrupted supply of electricity as long as a supply of methanol and water can be maintained. In addition, the energy storage density per unit volume/weight of this system is higher than that of batteries, which leads to less frequent recharging through the refilling of fuel.

Recently, a number of studies have been performed on the micro-reformer using methanol as fuel for portable PEMFC applications. Reuse et al.² found that the micro-reactors are much more suitable for the distributed production of hydrogen compared to the conventional systems. The channel width of the micro channels used in a micro-reformer ranges within 0.1–1.0 mm.^{3,4} Hessel et al.⁵ observed that the large surface/volume ratios in the microreformers lead to good heat- and mass-transfer properties and, hence, process intensification. These properties offer clear advantages, such as high mass- and heat-transfer rates, which are beneficial for attaining high selectivity and catalytic conversion and, hence, enable

*To whom correspondence should be addressed: Department of Aeronautics and Astronautics, National Cheng Kung University, No. 1, Ta Shieh Road, Tainan, Taiwan 70101, Republic of China. Telephone: 886-6-2757575 ext. 63627. Fax: 886-6-2389940. E-mail: chcheng@mail.ncku.edu.tw.

(1) Yu, X.; Tu, S. T.; Wang, Z.; Qi, Y. *Chem. Eng. J.* **2006**, *101*, 123–132.

(2) Reuse, P.; Penken, A.; Hass-Santo, K. *Chem. Eng. J.* **2004**, *101*, 133–141.

(3) Gobby, D.; Eames, I.; Gavrilidis, A. Proceedings of the Fifth International Conference of Microreaction Technology, Strasbourg, France, 2001; pp 142–149.

(4) Tonkovich, A. Y.; Zika, J. L.; LaMont, M. J. *Chem. Eng. Sci.* **2001**, *54*, 2947–2951.

(5) Hessel, V.; Ehrfeld, W.; Golbig, K. Proceedings of the Third International Conference of Microreaction Technology, Frankfurt, Germany, 2000; pp 526–540.

optimum control of temperature and residence time.^{6–8} Pfeifer et al.⁹ fabricated a microstructured reactor with small channels (0.1×0.1 mm), and a washcoating procedure of applying dispersed ZnO nanoparticles to the channel walls was adapted to the PdZn catalyst system. In addition, the Pacific Northwest National Laboratory (PNNL) has demonstrated a 40 W equivalent small-scale fuel processor consisting of a vaporizer, steam reformer, and recuperative heat exchanger.¹⁰ Motorola Laboratories disclosed an integrated fuel cell system with a ceramic methanol processor comprising fuel vaporizer, heat exchanger, reformer, and catalytic combustor. The system had been operated for 1 week, generating 0.7 W of electrical power by Hallmark.¹¹ A microreformer was fabricated by Park et al.¹² with dimensions of $70 \times 40 \times 30$ mm, concerning steam reforming of methanol, and authors found that the fuel processor generates enough hydrogen for power output of 15 W. On the basis of the previous studies, it is recognized that the performance of the micro-reformer strongly depends upon the catalyst coating, thermal management, reactor integration, and the channel designs for all of the components of a reactor.

In general, all of the reactor components, including vaporizer, combustor, and steam reformer, are equipped with flow channels for evenly distributing the reactant gases over the flow field for reaction because an even distribution of reactant gas over the flow field is a necessary condition for a higher reaction rate. However, the gas distribution is strongly dependent upon the flow network design. In a poor design, one may find that the channels close to the inlet or outlet manifolds receive more through flows than other channels. Therefore, the geometry of the manifold and the flow network should be accurately optimized toward even distribution of reactant gas. Accurate optimization is particularly important for the channels in a small-scale reactor component, whose characteristic length is usually only a few centimeters long. In these components, any small error in geometrical design may result in remarkable loss in the system performance. Therefore, the optimization of the geometry of the channels of the flow field cannot rely on the experiences of the designers only. An efficient computer-aided optimal design approach is definitely desirable to reduce the cost and time consumed during the design phase. Therefore, Pan et al.¹³ carried out an optimal design of complex manifold geometries for even flow distribution between microchannels by means of the flow network method. Tonomura et al.¹⁴ performed a CFD-based optimal design of the manifold in plate-fin microdevices. However, on the basis of the literature search, it appears that

relatively little work has been performed on the computational optimization of the three-dimensional geometry of the channels.

Under these circumstances, in this study, a computational optimization approach is presented and first applied to determine optimal combination of the channel widths of a micro-reformer to yield an even distribution of the reactant gases. Using the approach, automatic adjustment in sizes of the individual gas channels can be performed with the help of numerical simulation toward even gas flow distribution. The approach is developed by integrating a direct problem solver with an optimizer. A commercial computational fluid dynamics code (CFD-ACE+) is used as the direct problem solver to predict the three-dimensional mass and momentum transport phenomenon in the micro-reformer. On the other hand, the simplified conjugate-gradient method (SCGM) proposed by Cheng and Chang¹⁵ is employed as the optimizer, which works with the direct problem solver on the optimization of the channel width distribution. The SCGM method has been proven efficient as applied for the determination of irregular internal temperature distribution in PEMFC¹⁶ and optimization of the geometrical parameters of the PEMFC^{17,18} because of its flexibility in the definition of the objective functions for different applications.

2. Direct Problem Solver

A practical case is considered in this study for examining the performance of the optimization approach. Figure 1 shows the configurations of manifolds and gas channels of a flow field that has three possible models regarding the inlet and outlet configuration, including (1) model 1, central inlet/central outlet; (2) model 2, right inlet/right outlet; and (3) model 3, right inlet/left outlet.

The size of the micro-reformer is $11 \times 11 \times 1.1$ mm. The flow field in the micro-reformer contains an inlet manifold, seven parallel straight channels (numbered as CH1–CH7), and an outlet manifold. The channels are 6.952 mm long, and the ribs are 0.762 mm thick. In the original design, the widths of the gas channels are uniformly set to be 0.762 mm for all of the channels. However, it is observed that the original design usually leads to an uneven flow distribution. In the present study, the original design is now used as the initial guess in the beginning of the optimization process. An optimal non-uniform width distribution leading to evenly distributed flow rates in the channels will then be obtained for each of the three configurations shown in Figure 1.

In the direct problem solver, the theoretical model is developed under the following assumptions: (1) The flow field is steady and isothermal. (2) The magnitude of the Knudsen number is well below 0.01 in terms of the channel width under ambient conditions. Therefore, the flow is continuous, and the Navier–Stokes equations are valid. (3) Because the magnitude of the Reynolds number in terms of inlet air velocity and the channel width is approximately only 18, the flow can be assumed to be laminar. (4) Fluid viscosity and density are assumed constant. (5) The gravity effect is neglected.

The governing equations for the flow field are expressed in the following:

Continuity equation:

$$\frac{\partial u}{\partial x} + \frac{\partial v}{\partial y} + \frac{\partial w}{\partial z} = 0 \quad (1)$$

(15) Cheng, C. H.; Chang, M. H. *Numer. Heat Transfer, Part B* **2003**, 489–507.

(16) Chang, M. H.; Cheng, C. H. *J. Power Sources* **2005**, 142, 200–210.

(17) Lin, H. H.; Cheng, C. H.; Soong, C. Y.; Chen, F.; Yan, W. M. *J. Power Sources* **2006**, 162, 246–254.

(18) Cheng, C. H.; Lin, H. H.; Lai, G. J. *J. Power Sources* **2007**, 165, 803–813.

(6) Kursawe, A.; Dietzsch, E.; Kah, S.; Hönicke, D.; Fichtner, M.; Schubert, K.; Wiessmeier, G. *Proceedings of the 3rd International Conference on Microreaction Technology*, Springer, Berlin, Germany, 2000; pp 213–223.

(7) Kestenbaum, H.; Lange de Oliveira, A.; Schmidt, W.; Schüth, F.; Ehrfeld, W.; Gebauer, K.; Löwe, H.; Richter, Th.; Lebedz, D.; Untiedt, I.; Züchner, H. *Ind. Eng. Chem. Res.* **2002**, 41, 710–719.

(8) Rebrov, E. V.; Duinkerke, S. A.; de Croon, M. H. J. M.; Schouten, J. C. *Chem. Eng. J.* **2003**, 93, 201–216.

(9) Pfeifer, P.; Schubert, K.; Liauw, M. A.; Emig, G. *Appl. Catal., A* **2004**, 270, 165–175.

(10) Patil, A. S.; Dubois, T. G.; Sifer, N.; Bostic, E.; Gardner, K.; Quah, M.; Bolton, C. *J. Power Sources* **2004**, 136, 220–225.

(11) Hallmark, J. *Fuel Cell Seminar*, Miami, FL, 2003.

(12) Park, G. G.; Seo, D. J.; Park, S. H.; Yoon, Y. G.; Kim, C. S.; Yoon, W. L. *Chem. Eng. J.* **2004**, 101, 87–92.

(13) Pan, M.; Tang, Y.; Pan, L.; Lu, L. *Chem. Eng. J.* **2008**, 137, 339–346.

(14) Tonomura, O.; Tanaka, S.; Noda, M.; Kano, M.; Hasebe, S.; Hashimoto, I. *Chem. Eng. J.* **2004**, 101, 397–402.

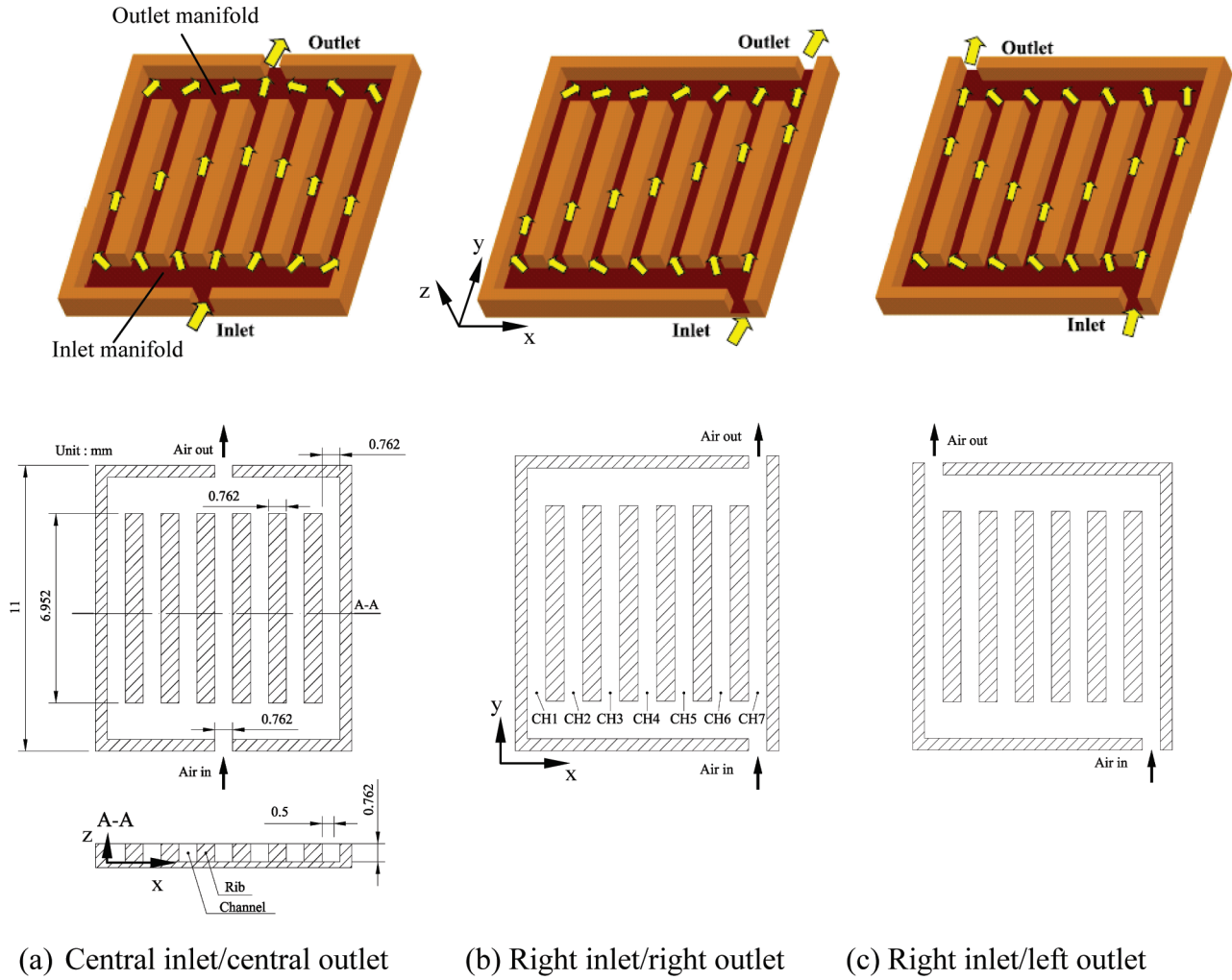


Figure 1. Configurations of manifolds and gas channels.

Momentum equations:

x direction:

$$u \frac{\partial(\rho u)}{\partial x} + v \frac{\partial(\rho u)}{\partial y} + w \frac{\partial(\rho u)}{\partial z} = -\frac{\partial p}{\partial x} + \frac{\partial}{\partial x} \left(\mu \frac{\partial u}{\partial x} \right) + \frac{\partial}{\partial y} \left(\mu \frac{\partial u}{\partial y} \right) + \frac{\partial}{\partial z} \left(\mu \frac{\partial u}{\partial z} \right) \quad (2)$$

y direction:

$$u \frac{\partial(\rho v)}{\partial x} + v \frac{\partial(\rho v)}{\partial y} + w \frac{\partial(\rho v)}{\partial z} = -\frac{\partial p}{\partial y} + \frac{\partial}{\partial x} \left(\mu \frac{\partial v}{\partial x} \right) + \frac{\partial}{\partial y} \left(\mu \frac{\partial v}{\partial y} \right) + \frac{\partial}{\partial z} \left(\mu \frac{\partial v}{\partial z} \right) \quad (3)$$

z direction:

$$u \frac{\partial(\rho w)}{\partial x} + v \frac{\partial(\rho w)}{\partial y} + w \frac{\partial(\rho w)}{\partial z} = -\frac{\partial p}{\partial z} + \frac{\partial}{\partial x} \left(\mu \frac{\partial w}{\partial x} \right) + \frac{\partial}{\partial y} \left(\mu \frac{\partial w}{\partial y} \right) + \frac{\partial}{\partial z} \left(\mu \frac{\partial w}{\partial z} \right) \quad (4)$$

where *u*, *v*, and *w* are the velocity components in the *x*, *y*, and *z* directions, respectively, and *p* denotes the fluid pressure.

The boundary conditions associated with the governing equations are as follows: (1) On the solid walls, the flow condition is assumed to comply with the nonpenetration and no-slip conditions on solid wall surfaces. (2) For all configurations, the inlet air velocity is fixed at 0.37 m/s. It means that the total entering flow

rate is kept constant in computation. At the outlet, the pressure is assigned to be 101.3 kPa.

The above set of conservation equations along with the boundary conditions and property equations are solved by adopting a finite-volume scheme within the framework of the commercial computational fluid dynamics code, CFD-ACE+. A grid-independence check has been performed to ensure the accuracy of the numerical solutions. In computation, the iteration for the solutions for *u*, *v*, *w*, and *p* is progressed until the following convergence criterion is satisfied:

$$|(\Psi'_{i,j,k} - \Psi'^{l-1}_{i,j,k}) / \Psi'^{l-1}_{i,j,k}| \leq 10^{-6} \quad (5)$$

where Ψ represents each of the variables, *u*, *v*, *w*, and *p*, *l* is the iteration number, and *i*, *j*, and *k* denote the grid indices in the *x*, *y*, and *z* directions, respectively.

In the optimization process, the widths of the channels are updated iteratively by the optimizer, which will be described in the following section. The grid generation unit CFD-GEOM is employed as the preprocessor to build the updated geometrical model and generate the grid system for computation. The direct problem solver is then used to predict the three-dimensional mass and momentum transport phenomenon and calculate the value of the objective function. It is noted that a careful check for the grid independence of the numerical solutions has been made prior to optimization to ensure the accuracy and validity of the numerical results. For this purpose, three grid numbers, 55 982, 102 025, and 152 359, are tested. It is found that the relative errors in the numerical predictions of the magnitudes of gas velocity between the solutions obtained by grids 102 025 and 152 359 are less than

2.0%. Therefore, the 102025 grid system is adopted in the computation considering the balance between computation time and accuracy.

3. Optimizer—SCGM Method

The SCGM method presented by Cheng and Chang¹⁵ is employed as the optimization scheme. This study is aimed at optimization of the widths of the channels, so that an even distribution of the flow rates in the channels can be obtained. Therefore, the objective function in conjunction with the optimization process is defined in the following:

$$P = \left\{ \left[\sum_{n=1}^7 (\dot{Q}_{CH_n} - \dot{Q}_{avg})^2 \right] \frac{1}{7} \right\}^{0.5} / \dot{Q}_{avg} \quad (6)$$

where \dot{Q}_{CH_n} denotes the volumetric flow rate in channel n , which is determined by integrating the cross-sectional velocity distribution with respect to the local area for each channel, and \dot{Q}_{avg} represents the average flow rate calculated by

$$\dot{Q}_{avg} = \left(\sum_{n=1}^7 \dot{Q}_{CH_n} \right) / 7 \quad (7)$$

The optimization of the flow channels is for evenly distributing the flow rates of the reactant gases over the flow field for reaction. Therefore, the flow rate and not the velocity is used to define the objective function. On the other hand, the widths of the seven channels are regarded as the parameters to the design, which are denoted by C_k , with $n = 1, 2, \dots, 7$. Note that the objective function is defined in terms of the standard deviation of flow rates in the seven channels. In this manner, the uniformity of the flow rates in the channels is expected to be greatly improved as the magnitude of the objective function (P) is minimized. The simplified conjugate-gradient method evaluates the gradients of the objective function and sets up a new conjugate direction for the updated solutions with the help of a sensitivity analysis. The initial guess for each designed parameter is made first, and in the successive steps, the conjugate-gradient coefficients and the searching directions are evaluated. The new design variables are continuously updated. When the objective function reaches a minimum, the optimization process is completed and the searching procedure is then terminated. In general, in a finite number of iterations, the convergence can be achieved. Because general descriptions and further details of the method are available in ref 15, the procedure of the optimization process for the present problem is described briefly as follows: (1) Make an initial guess for the widths of the seven channels $\{C_k, k = 1, 2, \dots, 7\}$. (2) Use the direct problem solver to predict the three-dimensional mass and momentum transport phenomenon and calculate the value of the objective function (P) by eq 5. When the objective function reaches a minimum, the solution process is terminated. Otherwise, proceed to step 4. (3) Perform the direct numerical sensitivity analysis to determine the gradient functions $(\partial P / \partial C_k)^n$ ($k = 1, 2, \dots, 7$). First, give a perturbation (ΔC_k) to each of the designed parameters $\{C_k, k = 1, 2, \dots, 7\}$, and then find the change in the objective function (ΔP) caused by ΔC_k . Then, the gradient function with respect to each of the designed parameters $\{C_k, k = 1, 2, \dots, 7\}$ can be calculated by the direct numerical differentiation as

$$\frac{\partial P}{\partial C_k} = \frac{\Delta P}{\Delta C_k} \quad (8)$$

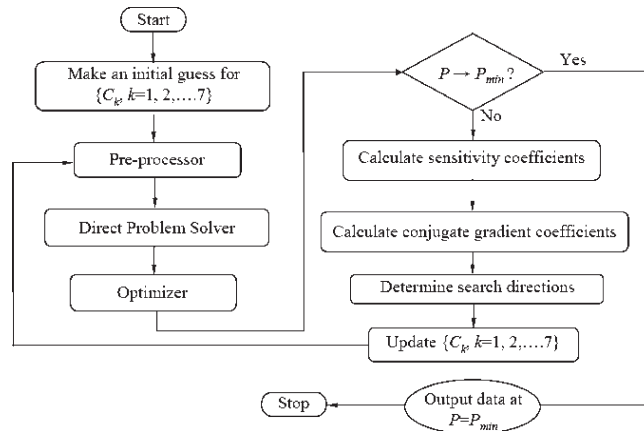


Figure 2. Flowchart of the optimization process.

(4) Calculate the conjugate gradient coefficients γ_k^n and the search directions π_k^{n+1} for each of the designed parameters $\{C_k, k = 1, 2, \dots, 7\}$ with

$$\gamma_k^n = \left[\frac{\left(\frac{\partial P}{\partial C_k} \right)^n}{\left(\frac{\partial P}{\partial C_k} \right)^{n-1}} \right]^2, \quad k = 1, 2, \dots, 7 \quad (9)$$

$$\pi_k^{n+1} = \left(\frac{\partial P}{\partial C_k} \right)^n + \gamma_k^n \pi_k^n, \quad k = 1, 2, \dots, 7 \quad (10)$$

The value of conjugate-gradient coefficients at $n = 0$ is typically set to zero as a start. (5) Assign values to the step sizes β_k ($k = 1, 2, \dots, 7$) for all of the designed parameters $\{C_k, k = 1, 2, \dots, 7\}$. Typically, those values are chosen within 0.01–0.001 after a trial-and-error process. (6) Update the widths of the seven channels ($C_k, k = 1, 2, \dots, 7$) with

$$C_k^{n+1} = C_k^n - \beta_k \pi_k^{n+1}, \quad k = 1, 2, \dots, 7 \quad (11)$$

and then go back to step 2.

Detailed information for determining the magnitudes of the perturbations (ΔC_k) and the step sizes (β_k) was described by Cheng and Chang.¹⁶ Here, in this study, the typical value for ΔC_k is assigned to be 0.00762 mm and the value of β_k is switched from 0.01, 0.005, and then to 0.001 in accordance with the convergence level in the optimization process. A smaller value of β_k is specified as the iterative design approaches the optimal solution.

The flowchart of the optimization process is plotted in Figure 2. The self-developed optimizer, the commercial CFD code, and the preprocessor are connected through an interface program. The interface program is written by Python language. Using the interface, it is possible to pass messages among the direct problem solver, the optimizer, and the preprocessor to update the geometrical model and generate a grid system for computation. The message of necessary changes in the designed parameters suggested by the optimizer is sent to the preprocessor for building the updated geometrical model and generating a grid system for computation. Next, the direct problem solver is executed on the basis of the updated information to yield the numerical predictions of the flow fields and the objective function as well, which are further transferred back to the optimizer for calculating the consecutive searching directions. The connection among the optimizer, the direct problem solver, and the preprocessor is shown in Figure 3.

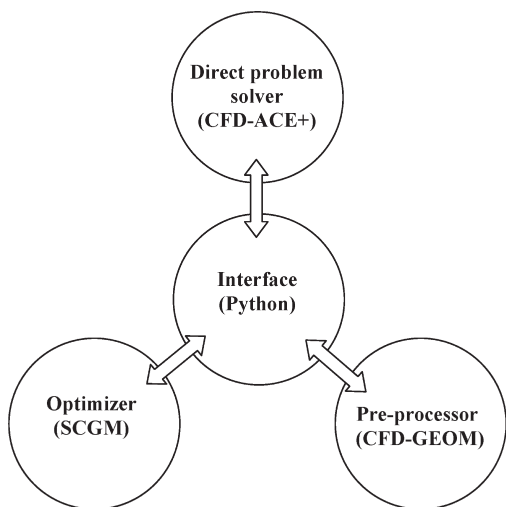


Figure 3. Connection among the optimizer, direct problem solver, and preprocessor.

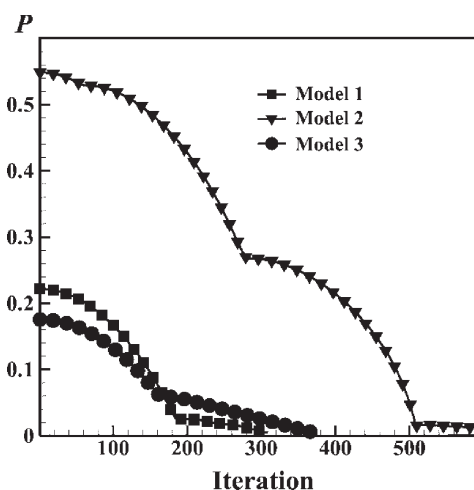


Figure 4. Convergence process of the objective function.

4. Results and Discussion

Figure 4 shows the variation in the objective function during the optimization process for the three models. It is seen that the value of the objective function is continuously decreased in the optimization process for all models. The numbers of iterations required to reach the optimal designs are roughly 300, 580, and 375 for models 1, 2, and 3, respectively. The iteration number with model 2 is larger than those with models 1 and 3. Also, it is found that the magnitude of the objective function of model 2 is always higher than those of models 1 and 3. This might be because, in model 2, both the inlet and outlet are placed on right-hand side of the flow field. With this asymmetrical configuration, it is more difficult to distribute the gas evenly to all of the channels than in the other two models. However, it is observed that, for the three models considered, the objective functions associated with models 1, 2, and 3 are reduced from 0.22, 0.55, and 0.18 to 0.005, 0.013, and 0.0068, respectively. As stated in point 2 above, the value of β_k is switched from 0.01, 0.005, and then to 0.001 in accordance with the convergence level in the optimization process. The jumps of the convergence process of the objective function in Figure 4 are caused when switching the value. The present approach leads to a significant decrease in the objective function for all three models.

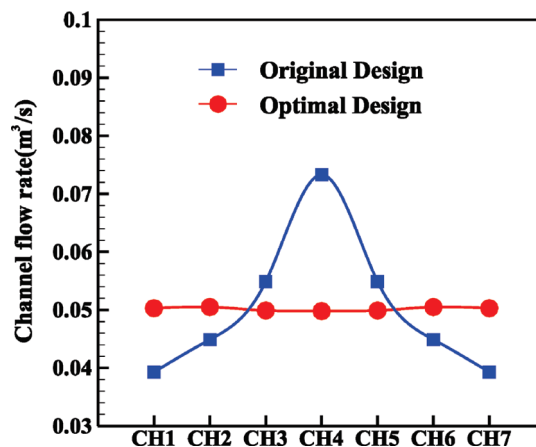
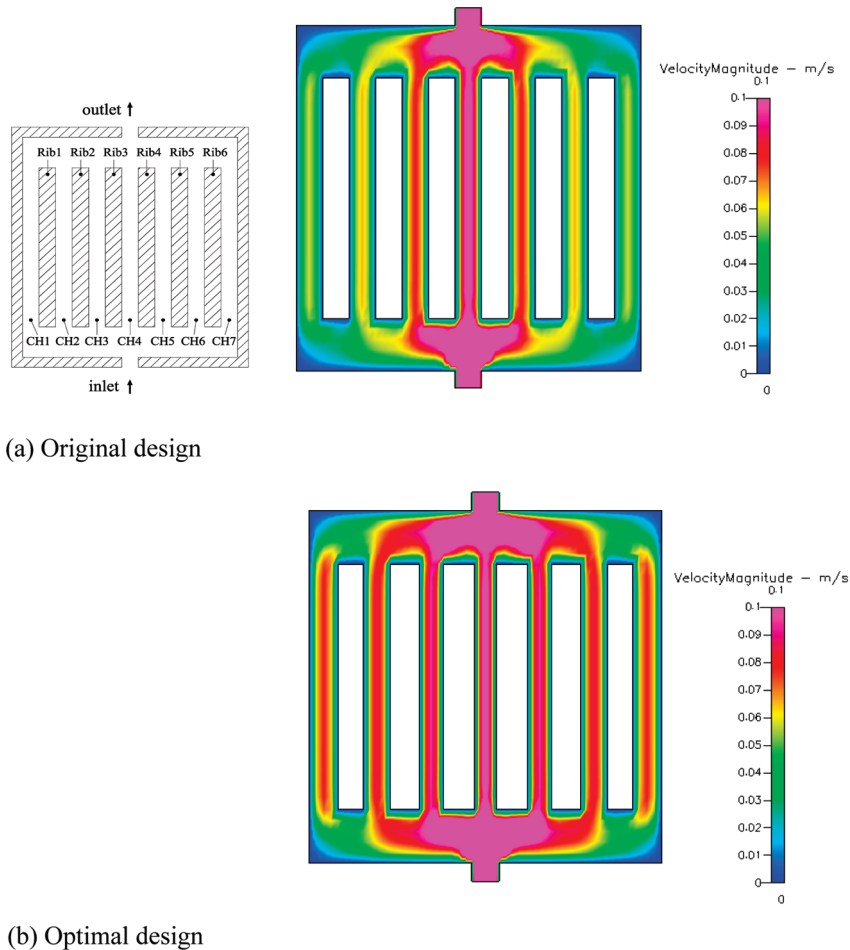


Figure 5. Distribution of the flow rate in the original and optimized channels, for model 1.

The improvement through optimization in the uniformity of flow distribution for model 1 is displayed in Figure 5. It is seen that in the original design the inlet and outlet of the flow are centered on the bottom and top walls of the flow field, respectively, and the widths of the gas channels are uniformly set to be 0.762 mm for all of the channels. As a result, in the original design, the flow is unevenly distributed. Higher flow rates are observed in the channels adjacent to the inlet. Among the seven channels, channel CH4 possesses the highest flow rate (0.074 m³/s), while channels CH1 and CH7 have much lower flow rates than other channels (less than 0.04 m³/s). However, the optimal design yielded by the present approach exhibits a rather even distribution. The total flow rate is shared out equally among the channels, and the flow rate in each channel is now 0.05 m³/s.

Detailed information regarding the optimal channel width distribution obtained with model 1 is provided in Figure 6. In the lower portion of this figure, the original and optimal channel width data are listed in a table. To improve the uneven flow rate distribution in the original design of model 1, the optimizer gradually increases the channel widths of CH1, CH2, CH6, and CH7 and reduces those of CH3, CH4, and CH5, so that the flow rates in the channels adjacent to the inlet can be decreased and those in the channels far from the inlet can be increased. In this manner, after the optimization process, an optimal distribution of the channel widths is obtained as 0.823, 0.765, 0.683, 0.597, 0.683, 0.765, and 0.823 mm, for channels CH1–CH7, respectively. Also plotted in this figure are the contour plots of the magnitude of the velocity vector (V) in the flow fields before and after optimization. Be aware that after optimization the flow rates in all of the channels are approximately the same value, 0.05 m³/s. Therefore, at the same flow rate, in a wider channel, the fluid velocity is expected to be lower and, on the contrary, in a narrower channel, the fluid velocity is higher. Figure 6b shows the velocity contours for the optimal design. Indeed, it is observed that the fluid velocity is slightly higher in the narrower channels (CH3, CH4, and CH5) than in the wider ones (CH1, CH2, CH6, and CH7). However, a comparison between panels a and b of Figure 6 illustrates that the velocities in the channels with the optimal design are much more uniform than those with the original design.

Plotted in Figure 7 are the distributions of flow rates in the channels with the original and optimized channels for model 2. In the original design of model 2, the widths of the gas



(Unit : mm)

Position	CH1	CH2	CH3	CH4	CH5	CH6	CH7
Original	0.762	0.762	0.762	0.762	0.762	0.762	0.762
Optimal	0.823	0.765	0.683	0.597	0.683	0.765	0.823

Figure 6. Velocity contours with flows before and after optimization, for model 1, at plane $z = 0.381$ mm.

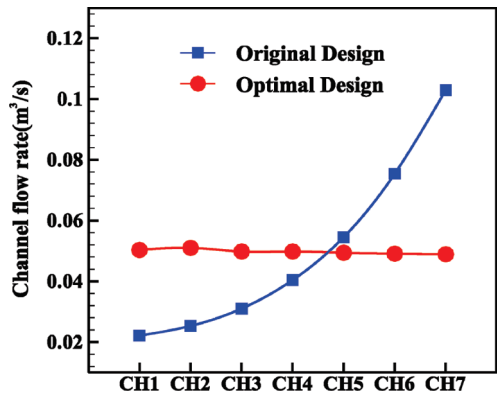
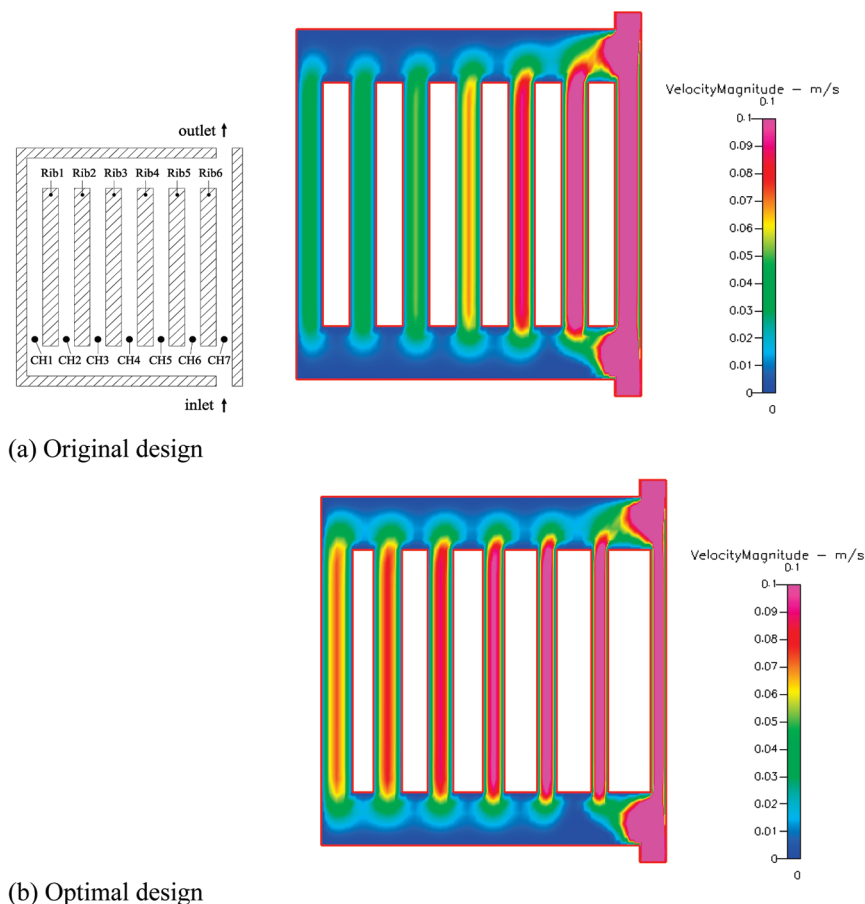


Figure 7. Distribution of the flow rate in the original and optimized channels, for model 2.

channels are uniformly set to be 0.762 mm for all of the channels, whereas the inlet and outlet of the flow are located at the right corners on the bottom and top walls, respectively. It is found that in the original design the flow rate is

monotonically increased from CH1 to CH7. In channel CH1, the flow rate is only $0.022 \text{ m}^3/\text{s}$, while in channel CH7, it reaches $0.103 \text{ m}^3/\text{s}$. Apparently, of the three models, this case is the most difficult to design. Nevertheless, as shown in Figure 7, the optimization process still achieves an optimal design, of which the flow rates in the channels are equal at $0.05 \text{ m}^3/\text{s}$. Numerical results for the optimal channel widths for the case are provided in Figure 8, which are 0.894, 0.826, 0.720, 0.628, 0.551, 0.489, and 0.443 mm for CH1–CH7, respectively. Again, in Figure 8b, for the optimal design, because the flow rates in the channels are equal, the fluid velocity is lower in a wider channel and higher in a narrower channel. Despite the difference in fluid velocity, the velocities in the channels with the optimal design are still much more uniform than those with the original design.

Figure 9 conveys the optimization results for the third model, model 3, in which the inlet is placed at the left corner on the bottom wall and the outlet at the right corner on the top wall. In the original model 3, channels CH1 and CH7 possess higher flow rates (0.066 and $0.062 \text{ m}^3/\text{s}$, respectively), while channel CH4 has the lowest flow rate ($0.042 \text{ m}^3/\text{s}$). After the



(Unit : mm)

Position	CH1	CH2	CH3	CH4	CH5	CH6	CH7
Original	0.762	0.762	0.762	0.762	0.762	0.762	0.762
Optimal	0.894	0.826	0.720	0.628	0.551	0.489	0.443

Figure 8. Velocity contours with flows before and after optimization, for model 2, at plane $z = 0.381$ mm.

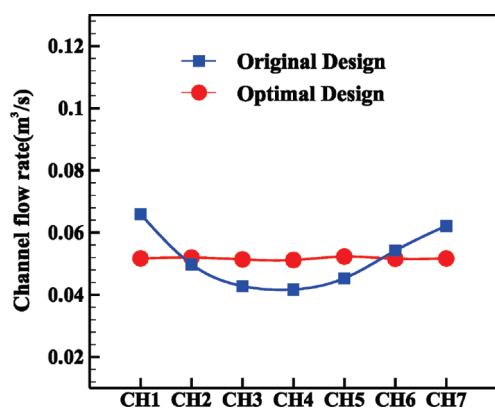


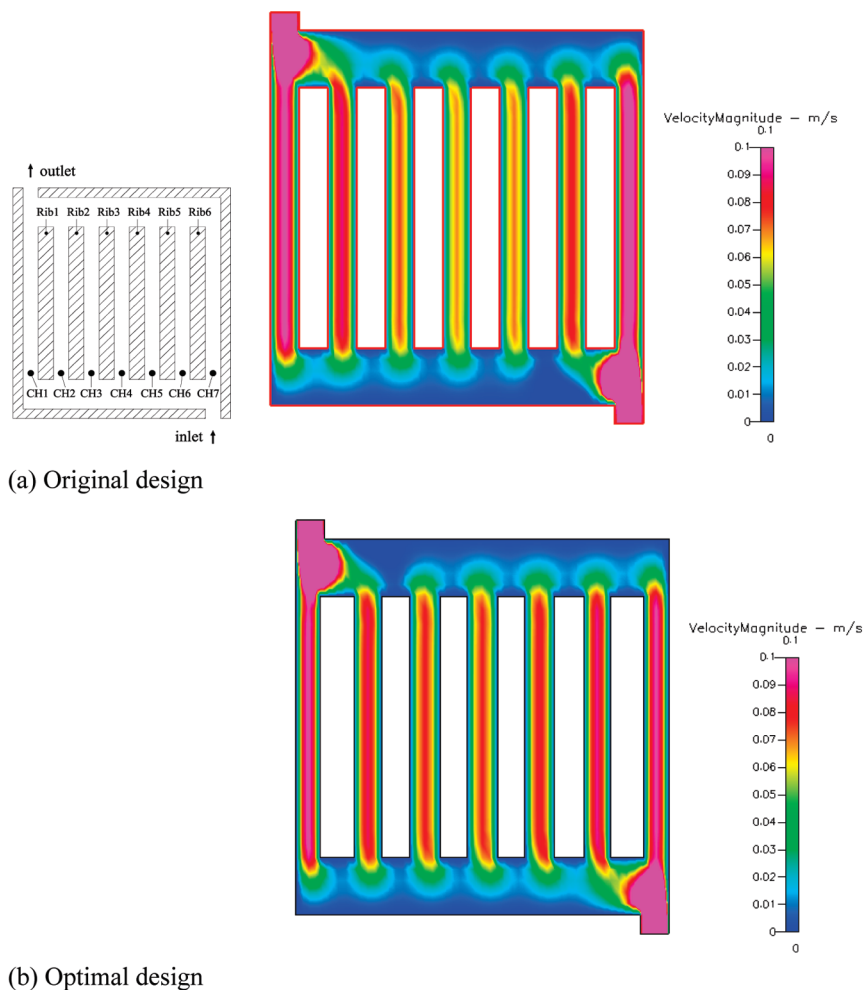
Figure 9. Distribution of the flow rate in the original and optimized channels, for model 3.

optimization process, the optimal design leads to an even flow rate distribution. For this case, the optimal combination of the channel widths is 0.644, 0.748, 0.812, 0.824, 0.789, 0.707, and 0.661 mm for CH1–CH7, respectively. The results are tabulated in Figure 10. Also, the velocity contours plots of the original and optimal designs for model 3 are presented in this

figure. A significant improvement in the fluid velocity distribution relative to the original design can also be observed.

In addition, at nearly equal flow rates in the optimized channels, the difference in channel widths leads to a difference in average channel velocities. These above figures provide sufficient information of the optimal and original channel widths and flow rates. One is able to calculate the differences in average velocity between the channels according to these data.

Another concern about the optimal design of the channel widths is how the process affects the pressure drop through the channels. Figure 11 shows the results for the pressure drops in the original and optimal designs for all three models. The pressure drop is calculated by the difference between the cross-sectional average pressures at the intake and exit of the channel. In general, the pressure drops in the channels are slightly increased after optimization. For example, the pressure drop in channel CH4 with the original design of model 1 is 0.389 N/m^2 . The magnitude of the pressure drop is increased to 0.448 N/m^2 with the optimal design of the same model. For model 2, maximal pressure drop with the original design is observed in channel CH7, which reads 0.555 N/m^2 . After optimization, the pressure drop in channel CH7 is increased to



(a) Original design

(b) Optimal design

(Unit : mm)

Position	CH1	CH2	CH3	CH4	CH5	CH6	CH7
Original	0.762	0.762	0.762	0.762	0.762	0.762	0.762
Optimal	0.644	0.748	0.812	0.824	0.789	0.707	0.661

Figure 10. Velocity contours with flows before and after optimization, for model 3, at plane $z = 0.381$ mm.

0.915 N/m². The increase in the pressure drop in CH7 caused by the optimization is 0.36 N/m². For all other models considered, the increase in the pressure drop is less than this value.

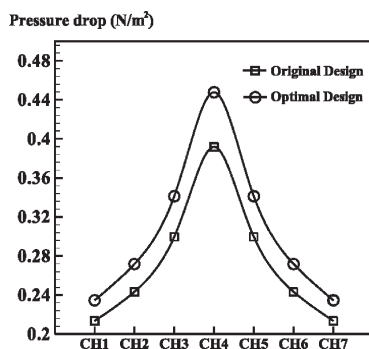
As already stated in the text, all of the reactor components, including vaporizer, combustor, and steam reformer are equipped with flow channels and an even distribution of reactant gas over the flow field is a necessary condition for a higher reaction rate. The present approach is essential and exactly matches the point required in elevating the performance of these devices. To justify the importance of the present approach on the fuel production, the chemical reaction model described in the Appendix is incorporated to predict the methanol conversion ratio and the hydrogen production rate for a micro steam reformer adopting the channels of model 1. Figure 12 displays the results for the mass fraction of methanol and the methanol conversion ratio in the steam-reforming process coming up with the present original and optimal designs for the micro reformer. It is found that the uniformity of the mass fraction of methanol

over the flow field can be greatly improved and the optimization indeed leads to even distribution of methanol mass fractions in the channels. As a result, the methanol conversion ratio is remarkably increased from 72.65 to 99.86%.

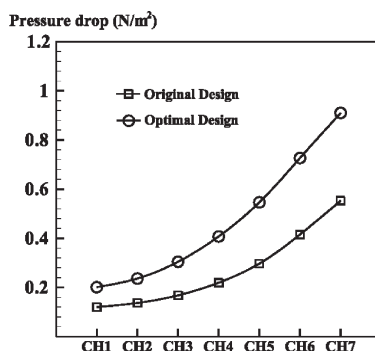
5. Concluding Remarks

In this study, a computational optimization approach has been developed by integrating the SCGM and a commercial computational fluid dynamics code through a Python-language interface. The approach has been first applied for optimization of the channel widths of an $11 \times 11 \times 1.1$ mm flow field to yield an even distribution of the reactant gases.

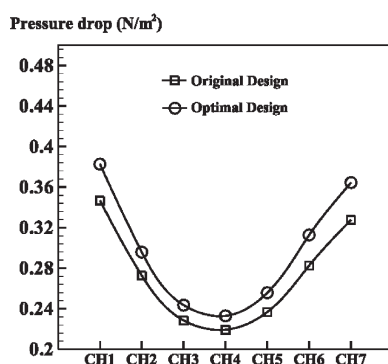
In the approach, an objective function is defined in terms of the standard deviation of the flow rates in the channels such that, as the magnitude of the objective function achieves a minimum value in the optimization process, the goal of evenly distributed flow rates in the channels can be reached successfully. It is found that the developed approach leads to a great improvement in the performance of the flow field with three



(a) Model 1



(b) Model 2



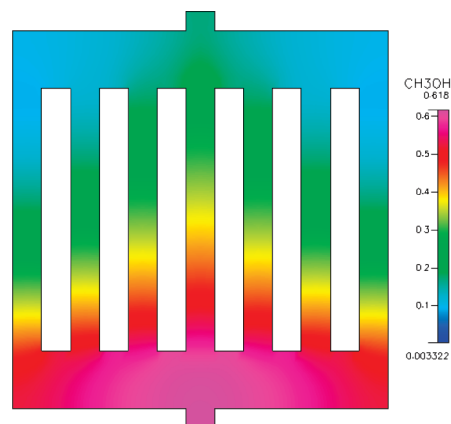
(c) Model 3

Figure 11. Pressure drop through channels.

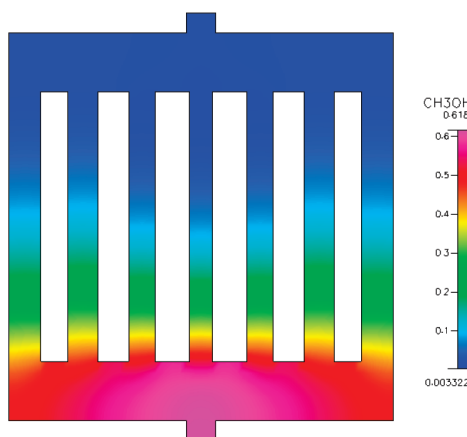
models regarding the inlet and outlet configuration, including (1) central inlet/central outlet, (2) right inlet/right outlet, and (3) right inlet/left outlet.

It is seen that the value of the objective function is continuously decreased in the optimization process for all models. The iteration number with model 2 is larger than those with models 1 and 3. Also, it is found that the magnitude of the objective function of model 2 is always higher than those of models 1 and 3. However, it is observed that, for the three models considered, the objective functions associated with models 1, 2, and 3 are reduced from 0.22, 0.55, and 0.18 to 0.005, 0.013, and 0.0068, respectively.

In addition, the pressure drops in the channels are slightly increased after optimization for all models. The highest increase in the pressure drop in the channels caused by the optimization is found with model 2. For this model, the pressure drop is increased by 0.36 N/m^2 . For all other models considered, the increase in the pressure drop is less than this value.



(a) Original design



(b) Optimal design

	Methanol conversion ratio
Original	72.65%
Optimal	99.86%

Figure 12. Distributions of the mass fraction and conversion ratios of methanol in the steam-reforming process before and after optimization, for model 1, at plane $z = 0.381 \text{ mm}$.

To justify the importance of the present approach on the fuel production, a chemical reaction model is incorporated to predict the methanol conversion ratio and the hydrogen production rate for a micro steam reformer adopting the channels of model 1. It is found that the methanol conversion ratio can be remarkably increased from 72.65 to 99.86%.

Appendix: Chemical Reaction Model

The governing equations for the chemical reaction are expressed as follows:

Continuity Equation.

$$\nabla(\varepsilon \rho v) = 0 \quad (\text{A1})$$

where ε is the porosity of the catalyst layer and ρ and v are the fluid density and velocity vector, respectively. For the pure fluid region, $\varepsilon = 1$.

Momentum Equations.

$$\nabla(\varepsilon\rho v) = -\varepsilon\nabla p + \nabla(\varepsilon\mu_{\text{mix}}\nabla v) + S_i \quad (\text{A2})$$

where p is the pressure and μ_{mix} is the dynamic viscosity of the gas mixture. The dynamic viscosity is determined on the basis of the Chapman–Enskog theory for multi-component gas mixtures at low density presented by Bird, Stewart, and Lightfoot.¹⁹ That is,

$$\mu_{\text{mix}} = \frac{\sum_{i=1}^{N_G} x_i \mu_i}{\sum_{j=1}^N x_j \Theta_{ij}} \quad (\text{A3-1})$$

and the dynamic viscosity of individual species is calculated by

$$\mu_i = 2.6693 \times 10^{-5} \frac{\sqrt{TM_i}}{\mathfrak{d}_i^2 \Omega_{\mu,i}} \quad (\text{A3-2})$$

where Ω_{μ} denotes a collision parameter calculated with

$$\Omega_{\mu} = \frac{1.16145}{T^{*0.14874}} + \frac{0.52487}{\exp(0.77320T^*)} + \frac{2.16178}{\exp(2.43787T^*)} \quad (\text{A3-3})$$

where $T^* = B/(Tk_B)$, with k_B being the Boltzmann constant in J/K and B being the maximum attractive energy between molecules. The Chapman–Enskog parameter Θ_{ij} in eq 14A3-1 is expressed as

$$\Theta_{ij} = \frac{1}{8} \left(1 + \frac{M_i}{M_j} \right)^{-1/2} \left[1 + \left(\frac{\mu_i}{\mu_j} \right)^{1/2} \left(\frac{M_j}{M_i} \right)^{1/4} \right]^2 \quad (\text{A3-4})$$

where M_i represents the molecular weight of species i .

In addition, in eq 13A2, the source term S_i only exists for the flow in the porous catalyst layer and is expressed as

$$S_i = -\frac{\varepsilon^2 \mu v}{k_p} - \frac{\varepsilon^3 C_F \rho}{\sqrt{k_p}} |v|v \quad (\text{A3-5})$$

where k_p is the permeability of the porous layer and C_F is the drag coefficient. Here, in the catalyst layer, $k_p = 2.379 \times 10^{-12} \text{ m}^2$ and $C_F = 0.55$. Note that, in the pure fluid region, $k_p = \infty$ and $S_i = 0$.

Energy Equation.

$$\nabla(\varepsilon\rho v h_0) = \nabla q + \varepsilon\tau\nabla v \quad (\text{A4})$$

where h_0 is the total enthalpy and τ is the shear stress tensor. The heat flux term q accounts for thermal conduction and energy transport by species diffusion, which is determined by

$$q = -k_{\text{mix}}\nabla T + \sum_{i=1}^{N_G} h_i J_i \quad (\text{A5-1})$$

where N_G is total number of gas-phase species and h_i is the specific enthalpy of species i . Thermal conductivity k_{mix} of the gaseous mixture is calculated using the kinetic theory¹⁹ and is written as

$$k_{\text{mix}} = \frac{\sum_{i=1}^{N_G} x_i k_i}{\sum_{j=1}^N x_j \Theta_{ij}} \quad (\text{A5-2})$$

The thermal conductivity of individual species can be calculated by

$$k_i = 1.9891 \times 10^{-4} \frac{\sqrt{T/M_i}}{\mathfrak{d}_i^2 \Omega_{\mu,i}} \quad (\text{A5-3})$$

Species mass flux J_i is composed of a concentration-driven term and a thermal-diffusion-driven term. That is,

$$J_i = J_i^C + J_i^T \quad (\text{A6})$$

where the concentration-driven species flux J_i^C is obtained from Fick's law of diffusion as follows:

$$J_i^C = -\rho D_i^C \nabla Y_i \quad (\text{A7-1})$$

where the concentration-driven diffusion coefficient of each species is expressed in terms of binary diffusion coefficients as

$$D_i^C = \frac{1-x_i}{\sum_{j=1, j \neq i}^{N_G} \frac{x_j}{D_{ij}}} \quad (\text{A7-2})$$

in which x_i is the mole fraction of species i and D_{ij} is multi-component diffusivity of the pair i – j determined by the Chapman–Enskog theory¹⁹ as

$$D_{ij} = 0.018583 \frac{\sqrt{T^3(M_i^{-1} + M_j^{-1})}}{\rho \mathfrak{d}_{ij}^2 \Omega_{D,ij}} \quad (\text{A7-3})$$

where \mathfrak{d}_{ij} is the Lennard–Jones collision diameter, which is calculated with

$$\mathfrak{d}_{ij}^2 = \frac{1}{2}(\sigma_i + \sigma_j) \quad (\text{A7-4})$$

with σ_i and σ_j representing the collision diameters of gas species i and j and

$$\Omega_{D,ij} = \frac{1.06036}{T^{*0.15610}} + \frac{0.19300}{\exp(0.47635T^*)} + \frac{1.03587}{\exp(1.52996T^*)} + \frac{1.76474}{\exp(3.89411T^*)} \quad (\text{A7-5})$$

On the other hand, the thermal-driven species flux is expressed by

$$J_i^T = -\rho D_i^T \nabla(\ln T) \quad (\text{A8-1})$$

where the thermal diffusion coefficient is calculated as follows:

$$D_i^T = \sum_{j=1, j \neq i}^{N_G} \frac{M_i M_j}{M^2} k_{ij} D_{ij} \quad (\text{A8-2})$$

with k_{ij} being the thermal diffusivity ratio.

Species Equation.

$$\nabla(\varepsilon\rho v Y_i) = \nabla J_i + S_c \quad (\text{A9})$$

where Y_i is the mass fraction of species i , and the species diffusion flux may be written in Maxwell–Stefan formulation as follows

$$J_i = \rho D_i \nabla Y_i + \frac{\rho Y_i}{M} D_i \nabla M - \rho Y_i \sum_j D_j \nabla Y_j - \rho Y_i \frac{\Delta M}{M} \sum_j D_j Y_j \quad (\text{A10-1})$$

In eq 31, S_c is the production rate of species i . In the reformer, the reactions are $\text{CH}_3\text{OH} + \text{H}_2\text{O} \rightarrow 3\text{H}_2 + \text{CO}_2$ and

(19) Bird, R. B.; Stewart, W. E.; Lightfoot E. N. *Transport Phenomena*; Wiley: New York, 1960.

$\text{CO}_2 + \text{H}_2 \rightarrow \text{CO} + \text{H}_2\text{O}$. Therefore, S_c can be determined by

$$S_c = R_{\text{SR}} + R_{\text{CO}} \\ = k_{\text{f,SR}} C_{\text{CH}_3\text{OH}}^{\alpha_{\text{SR,a}}} C_{\text{H}_2\text{O}}^{\alpha_{\text{SR,b}}} + k_{\text{f,CO}} C_{\text{CO}_2}^{\alpha_{\text{CO,a}}} C_{\text{H}_2}^{\alpha_{\text{CO,b}}} \quad (\text{A10-2})$$

where $\alpha_{\text{SR,a}}$, $\alpha_{\text{SR,b}}$, $\alpha_{\text{CO,a}}$, and $\alpha_{\text{CO,b}}$ are concentration exponents, and the chemical reaction rate coefficients, $k_{\text{f,SR}}$ and $k_{\text{f,CO}}$, can be expressed as follows:

$$k_{\text{f,SR}} = A_{\text{SR}} T^n (p/p_{\text{atm}})^m \exp(-E_{\text{a,SR}}/RT) \quad (\text{A10-3})$$

$$k_{\text{f,CO}} = A_{\text{CO}} T^n (p/p_{\text{atm}})^m \exp(-E_{\text{a,CO}}/RT) \quad (\text{A10-4})$$

where A , n , m , E_a , and R represent the pre-exponential constant, temperature exponent, exponent on pressure dependency, activation energy, and gas constant, respectively, whose values are reported by Pan and Wang.²⁰

Nomenclature

A = cross-sectional area of channels (m^2)
 A_{SR} and A_{CO} = pre-exponential constants
 C = design parameter/channel width
 C_F = drag coefficient
 C_i = concentration of the species i
 C_p = specific heat ($\text{kJ kg}^{-1} \text{K}^{-1}$)
 D = hydraulic diameter (m)
 D_i = multi-component diffusivity of species i (m^2/s)
 D_i^T = thermal diffusion coefficient of species i (m^2/s)
 D_{ij} = multi-component diffusivity of the pair i – j (m^2/s)
 E_a = activation energy (J/mol)
 h = specific enthalpy of formation (kJ/mol)
 J_i^C = concentration-driven species flux ($\text{kg m}^{-2} \text{s}^{-1}$)
 J_i^T = thermal-driven diffusive species flux ($\text{kg m}^{-2} \text{s}^{-1}$)
 J_i = species diffusion flux ($\text{kg m}^{-2} \text{s}^{-1}$)
 k_{mix} = conductivity for the gas mixture ($\text{W m}^{-1} \text{K}^{-1}$)
 k_p = catalyst layer permeability (m^2)
 k_{ij} = thermal diffusivity ratio
 k_{SR} and k_{CO} = chemical reaction coefficients
 L = channel length (m)
 m = exponent on pressure dependency
 M = molecular weight (kg/kmol)

n = temperature exponent
 N = total number of design parameters
 p = pressure (N/m^2)
 P = objective function
 q = heat flux (W/m^2)
 \dot{Q} = volumetric flow rate (m^3/s)
 R = universal gas constant ($\text{J mol}^{-1} \text{K}^{-1}$)
 S = direction of descent
 S_c = production rates of species i in the gas phase
 S_i = sources term of the pressure drop within porous media
 u = velocity component in the x direction (m/s)
 v = velocity component in the y direction (m/s)
 \vec{V} = velocity vector (m/s)
 w = velocity component in the z direction (m/s)
 x = mole fraction
 Y_i = mass fractions of species i
 x , y , and z = Cartesian coordinates (m)

Greek Symbols

α = concentration exponent
 β = step size
 γ = conjugate-gradient coefficients
 Θ_{ij} = Chapman–Enskog parameter
 μ = dynamic fluid viscosity (N s m^{-2})
 ρ = density of the fluid (kg/m^3)
 σ = Lennard–Jones parameter (Å)
 τ = shear stress tensor (N/m^2)
 ϖ = collision diameter (Å)
 Ω = collision integral

Subscripts

avg = average
 CH_n = number of channels
 i = grid index in the x direction
in = air inlet
 j = grid index in the y direction
 k = grid index in the z direction/index of the designed parameter
 l = iteration step in the flow field simulation
 n = iteration step in the optimization process
out = air outlet

(20) Pan, L.; Wang, S. *Chem. Eng. J.* **2005**, *108*, 51–58.